

# Parametric survey of longitudinal prominence oscillation simulations

Q. M. Zhang<sup>1,2</sup>, P. F. Chen<sup>1,3</sup>, C. Xia<sup>4</sup>, R. Keppens<sup>4</sup>, and H. S. Ji<sup>2</sup>

<sup>1</sup> School of Astronomy and Space Science, Nanjing University, 210093 Nanjing, PR China  
 e-mail: [zhangqm@pmo.ac.cn](mailto:zhangqm@pmo.ac.cn)

<sup>2</sup> Key Laboratory for Dark Matter and Space Science, Purple Mountain Observatory, CAS, 210008 Nanjing, PR China

<sup>3</sup> Key Lab of Modern Astronomy and Astrophysics, Ministry of Education, PR China

<sup>4</sup> Centre for mathematical Plasma Astrophysics, Department of Mathematics, KU Leuven, Celestijnenlaan 200B, 3001 Heverlee, Belgium

Received 8 November 2012 / Accepted 12 April 2013

## ABSTRACT

**Context.** Longitudinal filament oscillations recently attracted increasing attention, while the restoring force and the damping mechanisms are still elusive.

**Aims.** We intend to investigate the underlying physics for coherent longitudinal oscillations of the entire filament body, including their triggering mechanism, dominant restoring force, and damping mechanisms.

**Methods.** With the MPI-AMRVAC code, we carried out radiative hydrodynamic numerical simulations of the longitudinal prominence oscillations. We modeled two types of perturbations of the prominence, impulsive heating at one leg of the loop and an impulsive momentum deposition, which cause the prominence to oscillate. We studied the resulting oscillations for a large parameter scan, including the chromospheric heating duration, initial velocity of the prominence, and field line geometry.

**Results.** We found that both microflare-sized impulsive heating at one leg of the loop and a suddenly imposed velocity perturbation can propel the prominence to oscillate along the magnetic dip. Our extensive parameter survey resulted in a scaling law that shows that the period of the oscillation, which weakly depends on the length and height of the prominence and on the amplitude of the perturbations, scales with  $\sqrt{R/g_\odot}$ , where  $R$  represents the curvature radius of the dip, and  $g_\odot$  is the gravitational acceleration of the Sun. This is consistent with the linear theory of a pendulum, which implies that the field-aligned component of gravity is the main restoring force for the prominence longitudinal oscillations, as confirmed by the force analysis. However, the gas pressure gradient becomes significant for short prominences. The oscillation damps with time in the presence of non-adiabatic processes. Radiative cooling is the dominant factor leading to damping. A scaling law for the damping timescale is derived, i.e.,  $\tau \sim l^{1.63} D^{0.66} w^{-1.21} v_0^{-0.30}$ , showing strong dependence on the prominence length  $l$ , the geometry of the magnetic dip (characterized by the depth  $D$  and the width  $w$ ), and the velocity perturbation amplitude  $v_0$ . The larger the amplitude, the faster the oscillation damps. We also found that mass drainage significantly reduces the damping timescale when the perturbation is too strong.

**Key words.** Sun: filaments, prominences – Sun: oscillations – methods: numerical

## 1. Introduction

Solar prominences, or filaments that appear on the solar disk, are cold and dense plasmas suspended in the corona (Tandberg-Hanssen 1995; Labrosse et al. 2010; Mackay et al. 2010). They are formed above the magnetic polarity inversion lines. The denser material is believed to be supported by the magnetic tension force of the dip-shaped magnetic field lines (Kippenhahn & Schlüter 1957; Kuperus & Raadu 1974; Guo et al. 2010; Zhang et al. 2012; Xu et al. 2012; Su & van Ballegooijen 2012). These fascinating phenomena attracted many simulation efforts from different aspects, such as their formation, oscillations, and eruptions. For the formation, the chromospheric evaporation plus coronal condensation model has been studied widely with one-dimensional (1D) simulations (e.g., Müller et al. 2004; Karpen et al. 2005, 2006; Karpen & Antiochos 2008; Antolin et al. 2010; Xia et al. 2011; Luna et al. 2012b), where no back-reaction on the field topology is accounted for. This was for the first time extended to 2.5D by Xia et al. (2012), who simulated the in situ formation of a filament in a sheared magnetic arcade and showed that the condensation self-consistently forms magnetic dips while ensuring force-balance states. This finding strengthens the analysis performed for prominence formation and evolutions, as adopted by

many authors to date. Once a prominence is formed, it might be triggered to deviate from its equilibrium position and start to oscillate.

Observations demonstrate that prominences are hardly static. In addition to small-amplitude oscillations (Okamoto et al. 2007; Ning et al. 2009), large-amplitude and long-period prominence oscillations have been observed (e.g., Eto et al. 2002; Isobe & Tripathi 2006; Gilbert et al. 2008; Chen et al. 2008; Tripathi et al. 2009; Hershaw et al. 2011; Bocchialini et al. 2011). The observations of the prominence oscillations led to the comprehensive research topic of prominence seismology (Blokland & Keppens 2011a,b; Arregui & Ballester 2011; Arregui et al. 2012; Luna & Karpen 2012; Luna et al. 2012a), and the long-term oscillations were considered as one of the precursors for coronal mass ejections (CMEs; Chen et al. 2008; Chen 2011). Of particular interest in this paper are the longitudinal oscillations along the axis of prominences/filaments, which were first presented in the simulation results of Antiochos et al. (2000) discovered from H $\alpha$  observations by Jing et al. (2003). The phenomenon was investigated in more detail in Jing et al. (2006) and Vršnak et al. (2007). Such large-amplitude oscillations are triggered by small-scale solar eruptions near the footpoints of the main filaments, such as mini-filament eruptions, subflares, and flares. The initial velocities of the oscillations are 30–100 km s<sup>−1</sup>. The oscillation period ranges

from 40 min to 160 min and the damping times are  $\sim 2$ –5 times the oscillation period (Jing et al. 2006).

Unlike the transverse oscillations, whose restoring force is known to be the magnetic tension force, the dominant restoring force for the longitudinal oscillations still awaits to be clarified. Jing et al. (2003) proposed several candidates for the restoring force, i.e., gravity, pressure imbalance, and magnetic tension force. Vršnak et al. (2007) suggested that the restoring force is the magnetic pressure gradient along the filament axis. With radiative hydrodynamic simulations, Luna & Karpen (2012) and Zhang et al. (2012) suggested that the gravity component along the magnetic field is the main restoring force. Li & Zhang (2012), on the other hand, suggested that both gravity and magnetic tension force contribute to the restoring force. As for the damping mechanism, it really depends on the oscillation mode. For the vertical oscillations, Hyder (1966) proposed that the magnetic viscosity contributes to the decay. For the horizontal transverse oscillations, Kleczek & Kuperus (1969) proposed that the induced compressional wave in the surrounding corona acts to seemingly dissipate the oscillatory power. More damping mechanisms have been proposed, such as thermal conduction, radiation, ion-neutral collisions, resonant absorption, and wave leakage (see Tripathi et al. 2009 and Arregui et al. 2012, for reviews). For the longitudinal oscillations, Zhang et al. (2012) found that non-adiabatic terms such as the radiation and the heat conduction contribute to the damping, but they might not be sufficient to explain the observed shorter timescale. In their simulations the chromospheric heating was switched off, so that the prominence mass was nearly fixed. Conversely, Luna & Karpen (2012) studied the prominence oscillations while keeping the chromospheric heating and the resulting chromospheric evaporation. As a result, the prominence was growing in length and mass during oscillations. The authors found that there are two damping timescales, a short one for the initial stage and a longer one later. The analytical solution indicates that the mass accumulation can explain the fast damping of the initial state. For the later slower damping, they suggested non-adiabatic effects such as radiation and heat conduction. A quantitative survey is necessary to clarify how different geometrical and physical parameters of the prominence affect the damping timescale.

Within the framework of gravity serving as the restoring force for the longitudinal oscillations of the filament, in this paper we perform a parameter survey with the aim to clarify how the geometry of the magnetic field affects the oscillation period and how the combined effects of radiation and heat conduction contribute to the damping of the oscillations. We describe the numerical method in Sect. 2. After showing the effects of the perturbation type in Sect. 3, we display the results of our parameter survey in Sect. 4. Discussions and summary are presented in Sects. 5 and 6.

## 2. Numerical method

High-resolution observations indicate that a filament/prominence consists of many thin threads that are believed to be aligned to the individual magnetic tubes (Lin et al. 2005). Since the magnetic field inside the filament is quite strong (Schmieder & Aulanier 2012), the plasma beta is very low ( $\beta \sim 0.01$ – $0.1$ ) (Antiochos et al. 2000; DeVore & Antiochos 2000; Aulanier et al. 2006), and the thermal conduction is strongly prevented across the field lines, the dynamics inside different magnetic tubes can be considered to be independent. Therefore, the formation and evolution of a filament thread can be treated as a 1D hydrodynamic problem. Following Xia et al. (2011), the

1D radiative hydrodynamic equations, shown as follows, are numerically solved by the state-of-the-art MPI adaptive mesh refinement versatile advection code (MPI-AMRVAC; Keppens et al. 2003, 2012),

$$\frac{\partial \rho}{\partial t} + \frac{\partial}{\partial s}(\rho v) = 0, \quad (1)$$

$$\frac{\partial}{\partial t}(\rho v) + \frac{\partial}{\partial s}(\rho v^2 + p) = \rho g_{\parallel}(s), \quad (2)$$

$$\frac{\partial \varepsilon}{\partial t} + \frac{\partial}{\partial s}(\varepsilon v + p v) = \rho g_{\parallel} v + H - n_{\text{H}} n_{\text{e}} \Lambda(T) + \frac{\partial}{\partial s} \left( \kappa \frac{\partial T}{\partial s} \right), \quad (3)$$

where  $\rho$  is the mass density,  $T$  is the temperature,  $s$  is the distance along the loop,  $v$  is the velocity of plasma,  $p$  is the gas pressure,  $\varepsilon = \rho v^2/2 + p/(\gamma - 1)$  is the total energy density,  $n_{\text{H}}$  is the number density of hydrogen,  $n_{\text{e}}$  is the number density of electrons, and  $g_{\parallel}(s)$  is the component of gravity at a distance  $s$  along the magnetic loop, which is determined by the geometry of the magnetic loop. Furthermore,  $\gamma = 5/3$  is the ratio of the specific heats,  $\Lambda(T)$  is the radiative loss coefficient for the optically thin emission,  $H(s)$  is the volumetric heating rate, and  $\kappa = 10^{-6} T^{5/2} \text{ erg cm}^{-1} \text{ s}^{-1} \text{ K}^{-1}$  is the Spitzer heat conductivity. As in the previous works mentioned in Sect. 1, we assumed a fully ionized plasma and adopted a one-fluid model. Considering the helium abundance ( $n_{\text{He}}/n_{\text{H}} = 0.1$ ), we took  $\rho = 1.4 m_{\text{p}} n_{\text{H}}$  and  $p = 2.3 n_{\text{H}} k_{\text{B}} T$ , where  $m_{\text{p}}$  is the proton mass and  $k_{\text{B}}$  is the Boltzmann constant. The above equations are different from those in Luna & Karpen (2012) in that a uniform cross section was assumed here for the flux tube for simplicity, whereas expanding flux tubes based on given, immobile 3D magnetic fields were adopted in Luna & Karpen (2012). The radiative hydrodynamic Eqs. (1)–(3) were numerically solved with the MPI-AMRVAC code, where the heat conduction term is solved with an implicit scheme separately from other terms. To include the radiative loss, we interpolated with the second-order polynomial to compile a high-resolution table based on the radiative-loss calculations using updated element abundances and better atomic models over a wide temperature range (Colgan et al. 2008). The corresponding values in this table are systematically higher by almost two times than the previous radiative loss function adopted by Luna & Karpen (2012).

It is often believed that a prominence is hosted at the dip of a magnetic loop, supported by the magnetic tension force. Therefore, we adopted a loop geometry with a magnetic dip that is symmetric about the midpoint, as shown in Fig. 1. The loop consists of two vertical legs with a length of  $s_1$ , two quarter-circular shoulders with a radius  $r$  (the length of each arc,  $s_2 - s_1$ , is  $\pi r/2$ ), and a quasi-sinusoidal-shaped dip with a half-length of  $w$ . The height of the dip is expressed as  $y = D - D \cos(\pi x/2w)$  if the local coordinates  $(x, y)$  are centered at the midpoint of the dip. The dip has a depth of  $D$  below the apex of the loop. This geometry determines the field-aligned component of the gravity, whose distribution along the left half of the magnetic loop is expressed as follows:

$$g_{\parallel}(s) = \begin{cases} -g_{\odot}, & s \leq s_1; \\ -g_{\odot} \cos\left(\frac{\pi}{2} \frac{s - s_1}{s_2 - s_1}\right), & s_1 < s \leq s_2; \\ g_{\odot} \frac{\pi D}{2(L/2 - s_2)} \sin\left(\pi \frac{s - s_2}{L/2 - s_2}\right), & s_2 < s \leq L/2, \end{cases} \quad (4)$$

where the gravity at the solar surface  $g_{\odot} = 2.7 \times 10^2 \text{ m s}^{-2}$ , the total length of the loop  $L$ , the length of each vertical segment

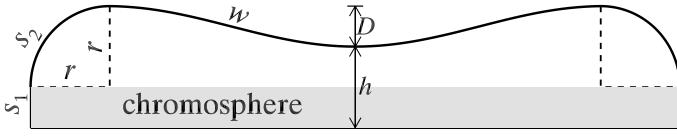


**Fig. 1.** Magnetic loop used for the 1D radiative hydrodynamic simulations of the prominence oscillations. The horizontal and the vertical sizes are not to scale.

$s_1 = 5$  Mm, and  $s_2 = s_1 + \pi r/2$  Mm. The total length of the dip is  $2w = L - 2s_2$ . The field-aligned component of the gravity in the right half is symmetric to the left half. The parameter  $h = s_1 + r - D$  gives the height of the central dip above the lower boundary.

Our simulations start from a thermal and force-balanced equilibrium state where the background heating is balanced by radiative loss and thermal conduction, and the plasma in the loop is quiescent. The simulations are divided into three steps. (1) Prominence formation: A prominence forms and grows near the center of the magnetic dip as chromospheric material is evaporated into the corona and condensates due to thermal instability after chromospheric heating is introduced near the footpoints of the loop. (2) Prominence relaxation: the prominence relaxes to a thermal and force-balanced equilibrium state as the localized heating is halted and the chromospheric evaporation ceases. (3) Prominence oscillation subjected to perturbations: The prominence starts to oscillate with a damping amplitude after perturbations are introduced. In step 1, which lasts for a time interval of  $\Delta t_1$ , the heating term  $H(s)$  in Eq. (3) is composed of two terms, the steady background heating  $H_0(s)$  and the localized chromospheric heating  $H_1(s)$ , which are expressed as follows:

$$H_0(s) = \begin{cases} E_0 \exp(-s/H_m), & s < L/2; \\ E_0 \exp[-(L-s)/H_m], & L/2 \leq s < L; \end{cases} \quad (5)$$

$$H_1(s) = \begin{cases} E_1, & s \leq s_{tr}; \\ E_1 \exp[-(s-s_{tr})/\lambda], & s_{tr} < s \leq L/2; \\ E_1 \exp[-(L-s_{tr}-s)/\lambda], & L/2 < s \leq L-s_{tr}; \\ E_1, & s > L-s_{tr}; \end{cases} \quad (6)$$

where the quiescent heating term  $H_0$  is adopted to maintain the hot corona with the amplitude  $E_0 = 3 \times 10^{-4}$  erg cm $^{-3}$  s $^{-1}$  and the scale-height  $H_m = L/2$ , and the localized heating term  $H_1$  is adopted to generate chromospheric evaporation into the corona with the amplitude  $E_1 = 10^{-2}$  erg cm $^{-3}$  s $^{-1}$ , the transition region height  $s_{tr} = 6$  Mm, and the scale height  $\lambda = 10$  Mm. The heating is taken to be symmetric so that it forms a static prominence near the magnetic dip center, so that we can easily control the manner how the prominence is triggered to oscillate. Our methodology is different from that in Luna & Karpen (2012), who used asymmetric heating that spontaneously leads to the oscillation once the prominence is formed. In step 2,  $H_1$  is switched off. Owing to the absence of the chromospheric evaporation, the gas pressure inside the magnetic loop drops, so the compressed prominence expands until a new equilibrium is reached, which takes less than approximately 2.4 h. In step 3, a perturbation is introduced to the prominence to trigger its oscillation. Note that  $H_0$  remains throughout the simulations.

From the observational point of view, there might be two types of perturbations. The first one is an impulsive momentum injected into the magnetic loop as the magnetic reconnection near the footpoints rearranges the magnetic loop rapidly. The second is impulsive heating due to subflares (e.g.,

Jing et al. 2003; Vrřnak et al. 2007; Li & Zhang 2012) or microflares (Fang et al. 2006) near the footpoints of the magnetic loop where a large amount of magnetic energy is impulsively released through magnetic reconnection. The gas pressure is greatly increased, which could propel the prominence to oscillate along the dip-shaped field lines. In our 1D simulations, we separated the two effects to see their difference. In one case, a velocity perturbation with the following distribution was imposed to the prominence,

$$v(s) = \begin{cases} 0, & s < s_{pl} - \delta; \\ v_0(s - s_{pl} + \delta)/\delta, & s_{pl} - \delta \leq s \leq s_{pl}; \\ v_0, & s_{pl} \leq s \leq s_{pr}; \\ v_0(-s + s_{pr} + \delta)/\delta, & s_{pr} \leq s \leq s_{pr} + \delta; \\ 0, & s > s_{pr}, \end{cases} \quad (7)$$

where  $s_{pl}$  and  $s_{pr}$  are the coordinates of the left and right boundaries of the prominence,  $\delta = 10$  Mm is the buffer zone that allows that the perturbation velocity varies smoothly in space, and  $v_0$  is the perturbation amplitude. In the other case, impulsive heating ( $H_2$ ), as described as follows, was introduced near the right-hand footpoint of the magnetic loop,

$$H_2(s) = E_2 \exp \left[ -\frac{(s - s_{peak})^2}{s_{scale}^2} - \frac{(t - t_{peak})^2}{t_{scale}^2} \right], \quad (8)$$

where the heating spatial scale  $s_{scale} = 2.5$  Mm, the peak location  $s_{peak} = 245$  Mm, the heating timescale  $t_{scale} = 5$  min, and the peak time  $t_{peak} = 15$  min. The heating increases to the peak for 15 min and then decreases to 0.

As for the boundary conditions, all variables at the two footpoints of the magnetic loop are fixed, which is justified because the density in the low atmosphere is more than four orders of magnitude higher than that in the corona. The same approach has been adopted by Ofman & Wang (2002) and Xia et al. (2011), assuming that the coronal dynamics has little effect on the low atmosphere. The approach was verified by Hood (1986) with the parameters being far from the marginal stability. The violation of the rigid wall conditions in certain cases was discussed by van der Linden et al. (1994).

### 3. Effects of the perturbation type

To check how the two types of perturbation described in Sect. 2 influence the characteristics of the prominence oscillations, we performed simulations of oscillations that are excited by the two types of perturbation while keeping  $\Delta t_1 = 7.2$  h,  $r = 20$  Mm,  $D = 10$  Mm, and  $L = 260$  Mm.

In case A, the prominence oscillation is triggered by a velocity perturbation over the whole prominence body. With  $v_0 = -40$  km s $^{-1}$  (the minus means that the velocity is toward the left), the temporal evolution of the plasma temperature distribution along the magnetic loop is displayed in the left panel of Fig. 2. In response to the perturbation, the prominence, signified by the low temperature, starts to oscillate around the equilibrium position. The oscillation amplitude decays with time. Fitting the trajectory of the mass center of the oscillating prominence with a decayed sine function

$$s = s_0 + A_0 \sin \left( \frac{2\pi}{P}t + \phi_0 \right) \exp(-t/\tau), \quad (9)$$

we find the initial amplitude  $A_0 = 34.9$  Mm, the oscillation period  $P = 84.3$  min, and the damping timescale  $\tau = 272$  min. Assuming that the prominence thread has a cross-section area of



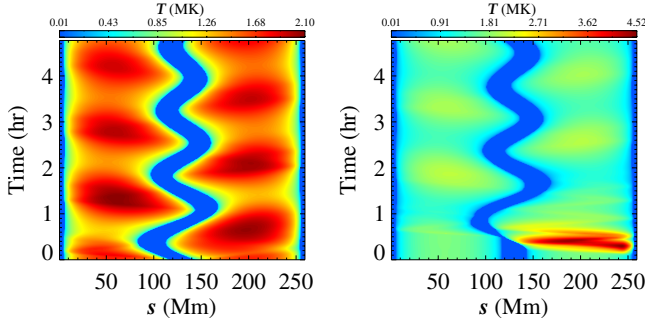


**Fig. 2.** Comparison of the evolutions of the loop temperature between the two types of perturbations. The *left panel* corresponds to the case with velocity perturbations with  $v_0 = -40 \text{ km s}^{-1}$  and the *right panel* to the case with localized heating perturbations with  $E_2 = 0.24 \text{ erg cm}^{-3} \text{ s}^{-1}$ .

$\sim 3.14 \times 10^{14} \text{ cm}^2$  (Lin et al. 2005), the initial kinetic energy of the oscillating prominence thread is estimated to be  $\sim 7.2 \times 10^{23} \text{ erg}$ . The single decayed sine function used for fitting the  $\text{H}\alpha$  observations (Jing et al. 2003; Vršnak et al. 2007; Zhang et al. 2012) fits the simulated observations very well. In contrast, a combination of Bessel function and an exponential decay function is necessary to fit the initial overtone in the simulations of Luna & Karpen (2012), which results from the continual mass accumulation.

In case B, the prominence oscillation was triggered by the impulsive heating that was deposited near the right leg of the magnetic loop to mimic a microflare near the prominence. To do this, an impulsive heating term  $H_2(s)$  in Eq. (8) was added to the heating term  $H$  in Eq. (3), where  $s_{\text{peak}} = 245 \text{ Mm}$ , meaning the heating is concentrated at a height of 15 Mm above the right footpoint of the magnetic loop.

The right panel of Fig. 2 depicts the temporal evolution of the temperature distribution along the magnetic loop with  $E_2 = 0.24 \text{ erg cm}^{-3} \text{ s}^{-1}$ . With the typical cross-section area of a prominence thread being  $\sim 3.14 \times 10^{14} \text{ cm}^2$ , the corresponding total energy deposited into the single magnetic loop  $E_{\text{heating}}$  is  $1.8 \times 10^{25} \text{ erg}$ . This value is reasonable since observations indicate that the total energy of a microflare is  $10^{26}$ – $10^{27} \text{ erg}$  or even more (e.g., Shimizu et al. 2002; Hannah et al. 2008; Fang et al. 2010), and several percent of the released energy dissipates into one prominence thread. From another point of view, in the framework of the magnetic reconnection model for microflares, the magnetic energy release rate is estimated to be  $B^2 v_{\text{in}} / (4\pi L)$ . With the magnetic field  $B \sim 20 \text{ G}$ , the reconnection inflow speed  $v_{\text{in}}$  being about 0.1 times the Alfvén speed, which is about  $1000 \text{ km s}^{-1}$  (Jiang et al. 2012), and the spatial size  $L = 10''$ , the energy release rate is estimated to be  $\sim 0.88 \text{ erg cm}^{-3} \text{ s}^{-1}$ , which is on the order adopted here. Fitting the trajectory of the oscillating prominence with the damped sine function as shown in Eq. (9) yields  $A_0 = 35.8 \text{ Mm}$ ,  $P = 84.3 \text{ min}$ , and  $\tau = 268 \text{ min}$ . The corresponding initial velocity is also  $-40 \text{ km s}^{-1}$ . This indicates that a typical microflare near the leg of the magnetic loop hosting a prominence thread can excite the prominence longitudinal oscillations with an initial velocity of tens of  $\text{km s}^{-1}$ . The corresponding kinetic energy is only  $\sim 7.2 \times 10^{23} / 1.8 \times 10^{25}$ , i.e.,  $\sim 4\%$  of the deposited thermal energy. The remaining  $\sim 96\%$  of the energy deposit contributes to the heating of the chromosphere.

#### 4. Parameter survey

The results in Sect. 3 reveal that the oscillation period does not strongly depend on the two types of perturbations, i.e., impulsive

momentum and localized heating at one footpoint used in our investigation. We concentrated on the oscillation characteristics that follow the short transient/excitation phase previously obtained from simple decaying sinusoidal fitting. A small difference in the decay timescale exists between the two perturbation types. With the same initial velocity, the decay timescale is 4 min shorter in the case of impulsive heating than that in the case of impulsive momentum. However, the relative variation, 1.4%, is very small. Therefore, we can conclude that the oscillation is basically intrinsic and the characteristics of the oscillation depend on the prominence itself and the geometry of the magnetic loop in our case without mass accumulation, and the oscillations are excited by either impulsive momentum or localized heating. The prominence feature is only characterized by the thread length ( $l$ ), and the geometry of the magnetic loop is characterized by  $r$ ,  $D$ , and  $w$  as depicted in Fig. 1. Among the three geometrical parameters,  $h = s_1 + r - D$  determines the height of the prominence,  $D$  and  $w$  determine the curvature of the magnetic dip. If other parameters are fixed, the length of the prominence is determined by the duration of the chromospheric evaporation in step 1, i.e.,  $\Delta t_1$ , as described in Sect. 2. Moreover, the decay timescale might vary with the perturbation amplitude, therefore another parameter is the initial perturbation velocity  $v_0$ . In this section, we perform a parameter survey to investigate how each of the five parameters ( $\Delta t_1$ ,  $r$ ,  $D$ ,  $w$ , and  $v_0$ ) changes the oscillation period and the decay timescale. For each parameter, several cases with different values are simulated with other parameters fixed. In our simulations, we set  $r = 10 \text{ Mm}$ ,  $D = 5 \text{ Mm}$ ,  $w = 110 \text{ Mm}$ , and  $v_0 = -20 \text{ km s}^{-1}$  when varying  $\Delta t_1$ . We set  $\Delta t_1 = 7.16 \text{ h}$ ,  $D = 5 \text{ Mm}$ ,  $w = 90 \text{ Mm}$ , and  $v_0 = -20 \text{ km s}^{-1}$  when varying  $r$ . We set  $\Delta t_1 = 7.16 \text{ h}$ ,  $D = 5 \text{ Mm}$ ,  $r = 10 \text{ Mm}$ , and  $v_0 = -20 \text{ km s}^{-1}$  when varying  $w$ . We set  $\Delta t_1 = 7.16 \text{ h}$ ,  $r = 20 \text{ Mm}$ ,  $w = 93.6 \text{ Mm}$ , and  $v_0 = -20 \text{ km s}^{-1}$  when varying  $D$ . We set  $\Delta t_1 = 7.16 \text{ h}$ ,  $r = 20 \text{ Mm}$ ,  $w = 93.6 \text{ Mm}$ , and  $D = 10 \text{ Mm}$  when varying  $v_0$ . Since the oscillation characteristics are found to be nearly insensitive to the perturbation type, we used the velocity perturbation to excite the oscillations in the survey.

##### 4.1. Length and mass of the prominence

After finishing the first two steps of the simulations as described in Sect. 2, we obtained a quasi-static prominence. The dependence of the prominence length  $l$  on  $\Delta t_1$ ,  $h$ ,  $D$ , and  $w$  is shown in the four panels of the upper row of Fig. 3. It can be seen that  $l$ , which fits into the scaling law  $l \sim \Delta t_1^{0.70}$ , increases with the duration of the heating time  $\Delta t_1$ . This is expected because more chromospheric plasma is evaporated into the corona when  $\Delta t_1$  increases. The length  $l$  decreases with  $h$  as  $l \sim h^{-0.37}$ , which is probably because it takes a longer time for the more tenuous corona to condensate as the height of the magnetic dip increases, and therefore the effective heating time is shorter. The length  $l$  decreases with  $D$  as  $l \sim D^{-0.21}$ , which can be understood as the prominence becoming more compressed as the magnetic dip becomes deeper. However, the length of the prominence does not vary considerably with  $w$ . Of course,  $w$  should not be too small, otherwise thermal instability would not occur. The lengths of these simulated prominence threads are consistent with the reported values, i.e., tens of Mm (Lin et al. 2005).

The dependence of the prominence mass  $M$  on  $\Delta t_1$ ,  $h$ ,  $D$ , and  $w$  is shown in the four panels of the lower row of Fig. 3. The dependence of  $M$  on  $\Delta t_1$ ,  $h$ , and  $w$  is similar to  $l$ . Their difference is that  $l$  decreases with  $D$  whereas  $M$  does not change with  $D$ , which means that the plasma number density ( $10^{10}$ – $10^{11} \text{ cm}^{-3}$ ,

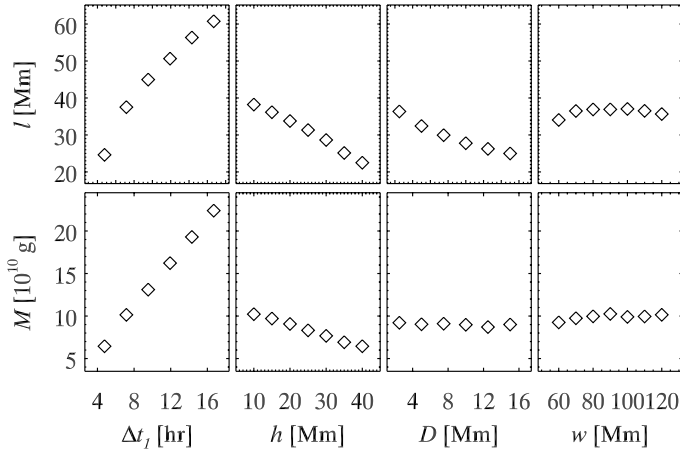


**Fig. 3.** Scatter plots of the total length  $l$  (upper panels) and mass  $M$  (lower panels) of the prominences at the end of relaxation step as functions of  $\Delta t_1$ ,  $h$ ,  $D$ , and  $w$ .

and the corresponding density is  $10^{-14}$ – $10^{-13}$  g cm $^{-3}$ ) is higher in the prominence with a deeper magnetic dip. A scaling law is obtained by fitting the data points, which is  $M \sim \Delta t_1^{0.98} h^{-0.34}$ .

The above results are derived for a dipped magnetic loop filled via chromospheric evaporation with a limited lifetime, where the prominence thread can be sustained in the corona. For magnetic loops without a dip (e.g., Mendoza-Briceño et al. 2005) or with a shallow dip and asymmetric heating (e.g., Karpen et al. 2006), condensations repetitively form, stream along the magnetic field, and ultimately disappear after falling back to the nearest footpoint. Therefore, the mass and length of the prominence evolve dynamically, without reaching an equilibrium value.

#### 4.2. Oscillation period and decay timescale

As the velocity perturbation is introduced to the quasi-static prominence, the prominence starts to oscillate. Fitting the trajectory of the oscillating prominence with the damped sine function shown in Eq. (9), we obtain the oscillation period ( $P$ ) and the decay timescale ( $\tau$ ) for each case in the parameter survey.

The variations of  $P$  along with the parameters  $l$ ,  $h$ ,  $D$ ,  $w$ , and  $v_0$  are shown in the upper row of Fig. 4.  $P$  increases slightly with  $l$  and  $v_0$ , and decreases slightly with  $h$ . However, it increases significantly with  $w$  and decreases with  $D$ . To fit the variations with a scaling law, we obtain  $P \sim l^{0.16} h^{-0.05} D^{-0.54} w^{0.91} v_0^{0.05}$ . Therefore, the period of the prominence longitudinal oscillations relies dominantly on the geometry of the dip, especially its curvature. The range of  $P$  agrees with the reported values in previous studies (e.g., Jing et al. 2006).

The variations of  $\tau$  along with the five parameters are shown in the lower row of Fig. 4.  $\tau$  increases significantly with  $l$  and  $D$ , and decreases with  $w$  and  $v_0$ . In the cases of  $|v_0| = 70$  and  $80$  km s $^{-1}$ , part of the prominence mass drains down to the chromosphere, which is why the triangles in the lower-right panel of Fig. 4 do not follow the trend of the data points denoted by the diamonds where  $|v_0| < 70$  km s $^{-1}$ . The decay timescale does not vary significantly with  $h$ . To fit the variations with a scaling law, we obtain  $\tau \sim l^{1.63} h^{-0.18} D^{0.66} w^{-1.21} v_0^{-0.30}$ , where the cases with prominence drainage are not included in the fitting. The values of  $\tau$  are also in the same order of magnitude as the observed ones.

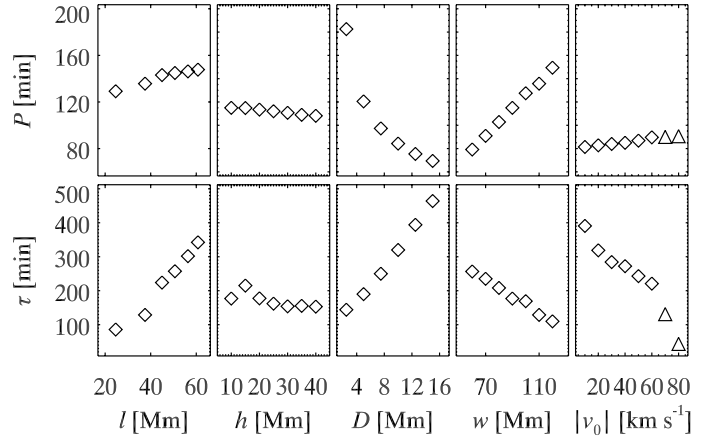


**Fig. 4.** Scatter plots of the period  $P$  (upper panels) and damping time  $\tau$  (lower panels) of the prominences in the oscillation step as functions of  $l$ ,  $h$ ,  $D$ ,  $w$ , and  $v_0$ . The values of  $P$  and  $\tau$  in the cases  $|v_0| = 70$  and  $80$  km s $^{-1}$  that cause mass drainage at the footpoint of the coronal loop are marked with triangles in the right panels.

## 5. Discussions

### 5.1. Restoring force

For an oscillating phenomenon, it is most important to determine the restoring force, which directly decides the oscillation period. In our 1D hydrodynamic simulations, the only forces exerted on the prominence are the gravity and the gas pressure gradient, both are restoring forces for the longitudinal oscillations. To compare their importance, we calculated the two forces in the case with  $\Delta t_1 = 7.16$  h,  $v_0 = -40$  km s $^{-1}$ ,  $r = 20$  Mm,  $D = 10$  Mm, and  $w = 93.6$  Mm. The two forces were calculated when the prominence is the farthest from the equilibrium position. Although the plasma in prominences is hundreds of times denser than the ambient corona, it is not an ideal rigid body. For oscillations with higher modes, as studied by Luna et al. (2012a), the pressure gradient changes rapidly along the prominence thread. For the fundamental-mode oscillations in this paper, the prominence oscillates as a whole and the pressure gradient changes slightly along the thread. Therefore, for simplicity, we compared the overall magnitude of the two forces by a simple calculation instead of point-to-point as in the simulations. The integral of the gravity force is quantified between the two ends of the prominence, i.e.,  $F_g = \int_{\text{left}}^{\text{right}} \rho |g_{\parallel}| ds = \int_{\text{left}}^{\text{right}} \rho g_{\odot} \frac{\pi D}{2w} |\sin(\frac{\pi(s-L/2)}{w})| ds$ , where a unit area is assumed for the cross section. The integral of pressure gradient force over the prominence is expressed as  $F_p = \int_{\text{left}}^{\text{right}} |\partial p / \partial s| ds = |p_{\text{right}} - p_{\text{left}}|$ . The left and right boundaries of the prominence are defined to be where the density drops to  $7 \times 10^{-14}$  g cm $^{-3}$ . Figure 5 displays the temporal evolution of the ratio  $F_g / F_p$ , from which it is seen that the gravitational force is generally about ten times stronger than the gas pressure gradient force.

Since the gravity is the dominant restoring force, the overall motion of the prominence can also be described for simplicity as

$$M \frac{d^2 x}{dt^2} = M g_{\parallel} = -M g_{\odot} \frac{\pi D}{2w} \sin\left(\frac{\pi x}{w}\right), \quad (10)$$

where  $x = s - L/2$  is the displacement of the prominence from the equilibrium position. It is not easy to solve this equation analytically. However, if the oscillation amplitude is much smaller than the half-width of the whole magnetic dip ( $w$ ), we derive the

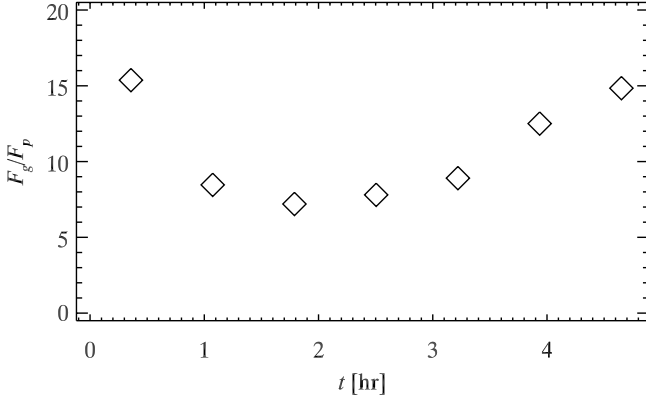


**Fig. 5.** Temporal variation of  $F_g/F_p$  when the displacement of the prominence reaches maximum during each half-cycle for  $r = 20$  Mm and  $D = 10$  Mm. The velocity perturbation is  $-40 \text{ km s}^{-1}$ .

approximation  $\sin(\pi x/w) \approx \pi x/w$ . Accordingly, the above equation is simplified to be

$$M \frac{d^2 x}{dt^2} = -M g_\odot \frac{\pi D}{2w} \frac{\pi x}{w}, \quad (11)$$

with the solution  $x = A_0 \sin(\frac{2\pi}{P}t + \phi)$ . The corresponding period is

$$P = \sqrt{\frac{8w^2}{g_\odot D}}. \quad (12)$$

This period can also be readily obtained if the prominence is taken in analogy to a pendulum whose period is

$$P = 2\pi \sqrt{\frac{R}{g_\odot}}, \quad (13)$$

where  $R$  is the curvature radius of the dipped magnetic loop. With the shape of the loop being  $y = D - D \cos(\pi x/2w)$ , the curvature radius at the loop center is approximated to be  $R = 2w^2/(D\pi^2)$ . Substituting  $R$  into Eq. (13), we derive  $P = \sqrt{8w^2/(g_\odot D)}$ , the same as Eq. (12). Figure 6 compares the oscillation periods obtained from the hydrodynamic simulations (*diamonds*) and those estimated from Eq. (12) (*solid line*) when the two parameters,  $D$  and  $w$ , are changed. This shows that Eq. (12) is a very good approximation for estimating the period of the prominence longitudinal oscillation. Of course, it should be kept in mind that the derivation of Eq. (12) is based on the assumption that the dipped magnetic loop has a sinusoidal shape. More generally, the oscillation period is related to the local curvature radius  $R$  by the formula  $P = 2\pi \sqrt{R/g_\odot}$ , as also demonstrated by Luna & Karpen (2012).

Recently, Luna et al. (2012a) extended the theoretical analysis of longitudinal prominence oscillations by including the effect of the pressure gradient force. They found that the ultimate fundamental frequency of the oscillations is found from  $\omega_{\text{fund}}^2 = \omega_g^2 + \omega_s^2$ , where  $\omega_g$  and  $\omega_s$  stand for the gravity-driven and pressure-driven frequencies, respectively. The ratio of the two frequencies  $\omega_g^2/\omega_s^2 = R_{\text{lim}}/R$ , where  $R_{\text{lim}}$  denotes the critical value of the curvature radius ( $R$ ) of the magnetic dip. If  $R \ll R_{\text{lim}}$ , gravity dominates over pressure in the restoring force of longitudinal oscillations. The authors pointed out that the reported values of the curvature are low compared with  $R_{\text{lim}}$ , so that it is reasonable to ignore the effect of the pressure term

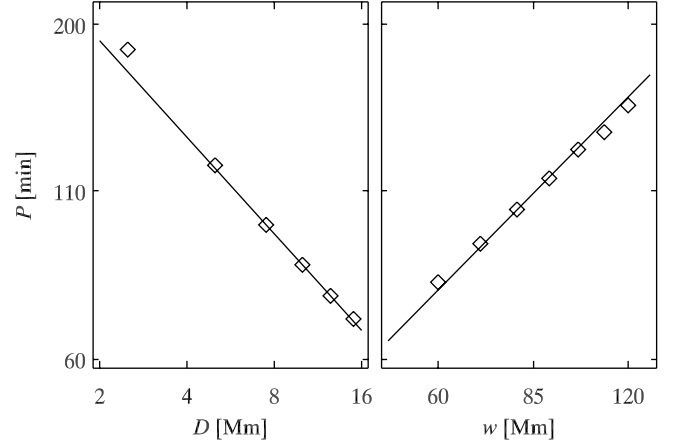


**Fig. 6.** Comparison of the periods of the prominence oscillations from simulations (*diamonds*) and theoretical analysis (*solid line*) as a function of the depth of the magnetic dip  $D$  (left panel) and the width of the dip  $w$  (right panel). Note that both axes are in logarithmic scale.

in most cases. In our parameter survey,  $R_{\text{lim}} = 0.175(L - l)$  ranges from 760 to 2100 Mm and the ratio  $R/R_{\text{lim}}$  ranges from 0.1 to 0.5. Hence, we confirm their theoretical results of gravity being the main restoring force for the fundamental mode in this parameter range.

For a prominence above the solar limb, all the parameters in Eq. (12) can be roughly measured. Combined with the results in this paper, the comparison between simulations and observations in Zhang et al. (2012) implies that Eq. (12) is a good approximation for estimating the oscillation period. For the prominence longitudinal oscillations on the solar disk, i.e., filament longitudinal oscillations, only the oscillation period can be unambiguously measured. Equation (12) then provides a diagnostic tool for inferring the geometry of the dipped magnetic loop. Especially when  $w$  can be roughly estimated from force-free magnetic extrapolations, the depth of the dip,  $D$ , can be determined. At least, we can estimate the curvature radius of the dipped magnetic field,  $R$ , through Eq. (13). After determining  $R$ , Luna & Karpen (2012) proposed an approximate method for estimating the magnetic field in the prominence.

In addition to the dominant dependence on the geometric parameters, the oscillation period also weakly changes with length and height of the prominence, as well as with the initial velocity. This can be understood as follows: (1) dependence on the prominence length: because the prominence thread is shorter, the ratio of the gas pressure gradient to the gravity would increase as indicated by our simulations, therefore, the gas pressure gradient would contribute to the restoring force, resulting in a shorter oscillation period. (2) Dependence on the prominence height: as seen from Fig. 3, with other parameters the same, a high prominence has a shorter length. Therefore, for the same reason as in (1), the oscillation period would be shorter. (3) Dependence on the initial velocity: since  $\sin(\pi x/w)$  is always smaller than  $\pi x/w$  in Eq. (10), the nonlinear term would naturally lead to a long period as the oscillation amplitude increases.

## 5.2. Damping mechanisms

When energy dissipation terms such as radiative cooling and heat conduction are removed from Eq. (3), as we did in a test simulation, we found that the prominence oscillation does not damp at all. When the two non-adiabatic terms are kept, the prominence oscillation always damps. To see the importance of



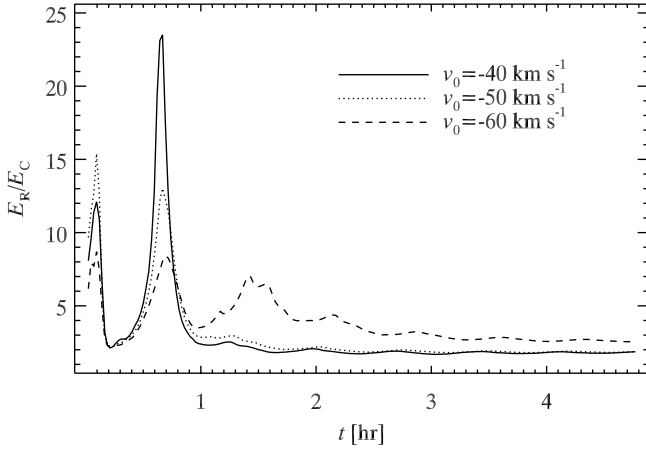


**Fig. 7.** Temporal variations of  $E_R/E_C$  in the oscillation step for  $v_0 = -40, -50$ , and  $-60 \text{ km s}^{-1}$ .

the two terms, we calculated the time integrations of radiative loss ( $E_R$ ) and thermal conduction ( $E_C$ ) of the whole system after subtracting the corresponding values when the prominence is static at the center of the dip. Here  $E_R$  and  $E_C$  are the integrals of the radiative and the conductive terms in the energy equation Eq. (3), where the integrals are taken in the whole corona above the two footpoints. The evolutions of the ratio ( $E_R/E_C$ ) for  $v_0 = -40, -50$ , and  $-60 \text{ km s}^{-1}$  are displayed in Fig. 7. The ratio is always higher than unity. Especially in the early stage of the oscillation when the amplitude is still large,  $E_R$  is even one order of magnitude larger than  $E_C$ . It is also revealed that as the initial velocity increases,  $E_R$  becomes increasingly important in most of the lifetime of the oscillation. Our results support the conclusions of Terradas et al. (2001, 2005) that radiative loss is responsible for the damping of the slow mode of prominence oscillations in the dip-shaped magnetic configurations, which seems to be different from the case of slow-mode waves propagating in the coronal loops where heat conduction contributes more to the damping (De Moortel et al. 2002a, 2002b).

The role of radiative cooling can be understood in a simple model as follows: since there are two segments of the corona in the magnetic loop, as the prominence oscillates, one part would be attenuated and the other be compressed. Assuming that the total length of the coronal part of the magnetic loop is unity, which includes part  $x$ , which is to the left of the prominence, and the other part  $1 - x$ , which is to the right of the prominence. Hence, the densities of the corona on the two sides are proportional to  $1/x$  and  $1/(1 - x)$ , respectively. The total optically thin radiative loss of the coronal part is proportional to  $x^{-2} + (1 - x)^{-2}$ , which is minimum when  $x = 0.5$ , i.e., when the prominence is situated at the equilibrium position. Whenever the prominence deviates from the loop center, the cooling becomes stronger, dissipating the kinetic energy of the oscillating prominence. The model is best illustrated by the relationship between the damping timescale ( $\tau$ ) and the initial amplitude of the oscillation, i.e.,  $A_0$  in Eq. (9). As  $A_0$  increases, one of the two coronal parts is more severely compressed, so the radiative cooling  $x^{-2} + (1 - x)^{-2}$  deviates more strongly from the lowest value, i.e., it becomes higher. As a result, the oscillation decays more rapidly.

Based on the sinusoidal function,  $A_0 \propto v_0 P$ . Substituting Eq. (12) into it, we obtain  $A_0 \propto v_0 w D^{-1/2}$ . With this, it is easy to understand the positive correlation between the decay timescale  $\tau$  and  $D$ , and the negative correlation between  $\tau$  and  $w$  as revealed by the lower row of Fig. 4. Along this line of thought, the dependence of the decay timescale on the prominence length

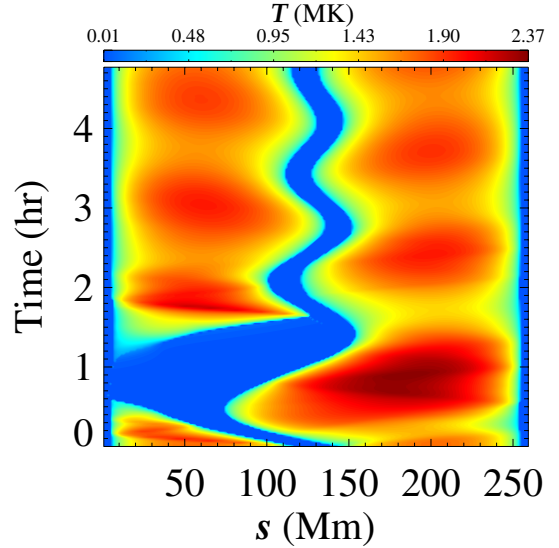


**Fig. 8.** Temporal evolution of the temperature along the magnetic loop when the initial velocity perturbation is as strong as  $v_0 = -80 \text{ km s}^{-1}$ . Note that the prominence passes the magnetic loop apex and drains down to the chromosphere at the left footpoint around  $t = 0.8 \text{ h}$ .

can be explained as follows: Because the prominence thread is longer, the coronal part of the magnetic loop, which radiates the thermal energy, is shorter. More importantly, the longer thread, with the same initial velocity, has a higher kinetic energy. Therefore, it takes a longer time for the compressed coronal part to radiate it.

The first six cases (i.e.,  $|v_0|$  from  $10 \text{ km s}^{-1}$  to  $60 \text{ km s}^{-1}$ ) in the lower-right panel of Fig. 4 show that the decay timescale decreases nearly linearly with the initial perturbation velocity. However, when  $v_0$  is higher than  $70 \text{ km s}^{-1}$ , part of the prominence would pass the magnetic loop apex and drain down. The critical velocity for the prominence to reach the loop apex can be roughly estimated as  $v_{\text{criti}} \sim \sqrt{2g_0 D} = 23 \sqrt{D/\text{Mm}} \text{ km s}^{-1}$ . Therefore, the value of  $v_{\text{criti}}$  is  $73 \text{ km s}^{-1}$  for  $D = 10 \text{ Mm}$ . As revealed from our simulations, even when  $v_0 = -70 \text{ km s}^{-1}$ , mass drainage happens, although the amount of the drainage is much lower than that for  $v_0 = -80 \text{ km s}^{-1}$ . The temperature evolution along the loop for  $v_0 = -80 \text{ km s}^{-1}$  is presented in Fig. 8. Part of the prominence falls down to the left leg of loop, leading to the drainage of the prominence mass and kinetic energy as well, while the remaining part continues to oscillate along the dip. The oscillation period and the decay timescale in the cases with mass drainage are marked as triangles in Fig. 4. Their periods,  $\sim 90.6 \text{ min}$ , are slightly shorter than the trend defined by other cases without mass drainage (*diamonds*), which is consistent with the weak positive correlation between  $P$  and the prominence length  $l$ . However, the damping timescales are greatly reduced compared to the trend defined by other cases without mass drainage, as seen from the lower-right panel of Fig. 4. This result, namely that mass drainage would greatly reduce the decay timescale, might explain the mismatch between the simulation and the observation of the decay of a prominence oscillation reported in Zhang et al. (2012).

## 6. Summary

In this paper, we carried out 1D hydrodynamic simulations of longitudinal prominence oscillations using the MPI-AMRVAC code, extending earlier numerical simulations of prominence

formation (Xia et al. 2011) and of prominence oscillations (Luna & Karpen 2012; Zhang et al. 2012). The simulations were divided into three steps: First, a prominence forms and grows near the center of the dip-shaped coronal loop due to chromospheric heating and the subsequent thermal instability. Then, it relaxes to a quiescent state after the chromospheric heating is switched off. Subjected to two types of perturbations that mimic sub-flares, the prominence starts to oscillate along the dip. Within the framework of the evaporation-condensation model, we obtained scaling-laws for the prominence length ( $l$ ) and mass ( $M$ ), which are expressed as  $l \sim \Delta t_1^{0.70} h^{-0.37} D^{-0.21}$  and  $M \sim \Delta t_1^{0.98} h^{-0.34}$ , where  $\Delta t_1$  is the time duration of the chromospheric heating and evaporation,  $h$  is the prominence height,  $D$  is the depth of the magnetic dip. We found that  $l$  is insensitive to the half length of the magnetic dip ( $w$ ) once  $w$  is large enough, about 60 Mm;  $M$  is insensitive to  $D$  and  $w$ . Both transient heating at one leg of the loop and an impulsive velocity perturbation applied to the prominence as a whole are capable of driving a coherent oscillation along the dip. The oscillation properties were found to be insensitive to the perturbation type in the regimes we studied. In the case of the transient heating,  $\sim 4\%$  of the deposited energy is converted into the kinetic energy of the prominence. The longitudinal oscillations are sustained mainly by the tangential component of gravity, except when the prominence is short and the gas pressure gradient becomes important as well. Both simulations and linear analysis revealed that the period of oscillation ( $P$ ) is  $2\pi\sqrt{R/g_\odot}$ , where  $R$  denotes the curvature radius of the dip, as also found by Luna & Karpen (2012). Other parameters, such as the length and height of the prominence, as well as the perturbation velocity, also affect  $P$ , though only slightly. The longitudinal oscillations damp in the presence of non-adiabatic effects, i.e., radiative loss and thermal conduction (Soler et al. 2009), among which radiative loss plays a leading role. With the parameter survey, we obtained a scaling-law for the decay timescale  $\tau$ , which is expressed as  $\tau \sim l^{1.63} D^{0.66} w^{-1.21} v_0^{-0.30}$ , where  $v_0$  is the initial velocity perturbation. We also found that prominence mass drainage, once it happens, significantly reduces the decay timescale, which may explain the mismatch between the simulations and the observations disclosed by Zhang et al. (2012).

These results are limited in application. According to this paper, the mass of a prominence thread is insensitive to the depth  $D$  and the width  $w$  of the magnetic dip. This is based on the prominence formation directly via chromospheric evaporation with a fixed lifetime  $\Delta t_1$ . According to Xia et al. (2011), the prominence would grow via siphon flow even when the localized heating is switched off, though the growth speed is much slower. Recently, Luna et al. (2012a) pointed out that the restoring force of the longitudinal oscillations depends on the depth of the magnetic dip. For shallow dips, gas pressure plays an important role, while gravity is the main factor for deep dips. Moreover, Li & Zhang (2012) suggested that magnetic tension may also contribute to the restoring force. As for the damping mechanisms, several other effects might need to be taken into account in the future simulations, such as the wave leakage and plasma viscosity (Ofman & Wang 2002). However, some will only be quantifiable in true multidimensional configurations, e.g., starting from the prominences formed in Xia et al. (2011).

**Acknowledgements.** The authors thank the anonymous referee for detailed and enlightening comments that improved the paper. Q. M. Zhang acknowledges C. Fang, M. D. Ding, W. Q. Gan, Y. P. Li, Z. J. Ning, S. M. Liu, D. J. Wu, H. Li, and L. Feng for discussions and suggestions throughout this work. R.K. acknowledges funding from the Interuniversity Attraction Poles Programme initiated by the Belgian Science Policy Office (IAP P7/08 CHARM). The research is supported by the Chinese foundations NSFC (11025314, 10878002, 10933003, and 11173062) and 2011CB811402.

## References

- Antiochos, S. K., MacNeice, P. J., & Spicer, D. S. 2000, *ApJ*, 536, 494  
 Antolin, P., Shibata, K., & Vissers, G. 2010, *ApJ*, 716, 154  
 Arregui, I., & Ballester, J. L. 2011, *Space Sci. Rev.*, 158, 169  
 Arregui, I., Oliver, R., & Ballester, J. L. 2012, *Liv. Rev. Sol. Phys.*, 9, 2  
 Aulanier, G., DeVore, C. R., & Antiochos, S. K. 2006, *ApJ*, 646, 1349  
 Blokland, J. W. S., & Keppens, R. 2011a, *A&A*, 532, A94  
 Blokland, J. W. S., & Keppens, R. 2011b, *A&A*, 532, A93  
 Bocchialini, K., Baudin, F., Koutchmy, S., Pouget, G., & Solomon, J. 2011, *A&A*, 533, A96  
 Chen, P. F. 2011, *Liv. Rev. Sol. Phys.*, 8, 1  
 Chen, P. F., Innes, D. E., & Solanki, S. K. 2008, *A&A*, 484, 487  
 Colgan, J., Abdallah, J., Jr., Sherrill, M. E., et al. 2008, *ApJ*, 689, 585  
 De Moortel, I., Ireland, J., Walsh, R. W., & Hood, A. W. 2002a, *Sol. Phys.*, 209, 61  
 De Moortel, I., Hood, A. W., Ireland, J., & Walsh, R. W. 2002b, *Sol. Phys.*, 209, 89  
 DeVore, C. R., & Antiochos, S. K. 2000, *ApJ*, 539, 954  
 Eto, S., Isobe, H., Narukage, N., et al. 2002, *PASJ*, 54, 481  
 Fang, C., Tang, Y.-H., & Xu, Z. 2006, *Chin. J. Astron. Astrophys.*, 6, 597  
 Fang, C., Chen, P.-F., Jiang, R.-L., & Tang, Y.-H. 2010, *Res. Astron. Astrophys.*, 10, 83  
 Gilbert, H. R., Daou, A. G., Young, D., Tripathi, D., & Alexander, D. 2008, *ApJ*, 685, 629  
 Guo, Y., Schmieder, B., Démoulin, P., et al. 2010, *ApJ*, 714, 343  
 Hannah, I. G., Christie, S., Krucker, S., et al. 2008, *ApJ*, 677, 704  
 Hershaw, J., Foullon, C., Nakariakov, V. M., & Verwichte, E. 2011, *A&A*, 531, A53  
 Hood, A. W. 1986, *Sol. Phys.*, 105, 307  
 Hyder, C. L. 1966, *ZAp*, 63, 78  
 Isobe, H., & Tripathi, D. 2006, *A&A*, 449, L17  
 Jiang, R.-L., Fang, C., & Chen, P.-F. 2012, *ApJ*, 751, 152  
 Jing, J., Lee, J., Spirock, T. J., Xu, Y., Wang, H., & Choe, G. S. 2003, *ApJ*, 584, L103  
 Jing, J., Lee, J., Spirock, T. J., & Wang, H. 2006, *Sol. Phys.*, 236, 97  
 Karpen, J. T., & Antiochos, S. K. 2008, *ApJ*, 676, 658  
 Karpen, J. T., Tanner, S. E. M., Antiochos, S. K., & DeVore, C. R. 2005, *ApJ*, 635, 1319  
 Karpen, J. T., Antiochos, S. K., & Klimchuk, J. A. 2006, *ApJ*, 637, 531  
 Keppens, R., Nool, M., Tóth, G., & Goedbloed, J. P. 2003, *Comput. Phys. Comm.*, 153, 317  
 Keppens, R., Meliani, Z., van Marle, A. J., et al. 2012, *J. Comput. Phys.*, 231, 718  
 Kippenhahn, R., & Schlüter, A. 1957, *Z. Astrophys.*, 43, 36  
 Kleczek, J., & Kuperus, M. 1969, *Sol. Phys.*, 6, 72  
 Kuperus, M., & Raadu, M. A. 1974, *A&A*, 31, 189  
 Labrosse, N., Heinzel, P., Vial, J.-C. et al. 2010, *Space Sci. Rev.*, 151, 243  
 Li, T., & Zhang, J. 2012, *ApJ*, 760, L10  
 Lin, Y., Engvold, O., Rouppe van der Voort, L., Wiik, J. E., & Berger, T. E. 2005, *Sol. Phys.*, 226, 239  
 Luna, M., & Karpen, J. 2012, *ApJ*, 750, L1  
 Luna, M., Díaz, A. J., & Karpen, J. 2012a, *ApJ*, 757, 98  
 Luna, M., Karpen, J. T., & DeVore, C. R. 2012b, *ApJ*, 746, 30  
 Mackay, D. H., Karpen, J. T., Ballester, J. L., Schmieder, B., & Aulanier, G. 2010, *Space Sci. Rev.*, 151, 333  
 Mendoza-Briceño, C. A., Sigalotti, L. D. G., & Erdélyi, R. 2005, *ApJ*, 624, 1080  
 Müller, D. A. N., Peter, H., & Hansteen, V. H. 2004, *A&A*, 424, 289  
 Ning, Z., Cao, W., Okamoto, T. J., Ichimoto, K., & Qu, Z. Q. 2009, *A&A*, 499, 595  
 Ofman, L., & Wang, T. 2002, *ApJ*, 580, L85  
 Okamoto, T. J., Tsuneta, S., Berger, T. E., et al. 2007, *Science*, 318, 1577  
 Schmieder, B., & Aulanier, G. 2012, *EAS PS*, 55, 149  
 Shimizu, T., Shine, R. A., Title, A. M., Tarbell, T. D., & Frank, Z. 2002, *ApJ*, 574, 1074  
 Soler, R., Oliver, R., & Ballester, J. L. 2009, *ApJ*, 693, 1601  
 Su, Y., & van Ballegoijen, A. 2012, *ApJ*, 757, 168  
 Tandberg-Hanssen, E. 1995, *Science*, 269, 111  
 Terradas, J., Oliver, R., & Ballester, J. L. 2001, *A&A*, 378, 635  
 Terradas, J., Carbonell, M., Oliver, R., & Ballester, J. L. 2005, *A&A*, 434, 741  
 Tripathi, D., Isobe, H., & Jain, R. 2009, *Space Sci. Rev.*, 149, 283  
 van der Linden, R. A. M., Hood, A. W., & Goedbloed, J. P. 1994, *Sol. Phys.*, 154, 69  
 Vršnak, B., Veronig, A. M., Thalmann, J. K., & Žic, T. 2007, *A&A*, 471, 295  
 Xia, C., Chen, P. F., Keppens, R., & van Marle, A. J. 2011, *ApJ*, 737, 27  
 Xia, C., Chen, P. F., & Keppens, R. 2012, *ApJ*, 748, L26  
 Xu, Z., Lagg, A., Solanki, S., & Liu, Y. 2012, *ApJ*, 749, 138  
 Zhang, Q. M., Chen, P. F., Xia, C., & Keppens, R. 2012, *A&A*, 542, A52